J. Fluid Mech. (2017), *vol.* 824, *pp.* 550–573. © Cambridge University Press 2017
This is an Open Access article, distributed under the terms of the Creative Commons Attribution licence (http://creativecommons.org/licenses/by/4.0/), which permits unrestricted re-use, distribution, and reproduction in any medium, provided the original work is properly cited.
doi:10.1017/jfm.2017.363

Pore-filling events in single junction micro-models with corresponding lattice Boltzmann simulations

Ioannis Zacharoudiou[1,†], Emily M. Chapman[1], Edo S. Boek[1,2] and John P. Crawshaw[1]

[1]Qatar Carbonates and Carbon Storage Research Centre, Department of Chemical Engineering, Imperial College London, South Kensington Campus, London SW7 2AZ, UK

[2]Soft Matter Research Group, Department of Applied Mathematics and Theoretical Physics, Centre for Mathematical Sciences, University of Cambridge, CB3 0WA, UK

(Received 24 November 2016; revised 3 April 2017; accepted 19 May 2017; first published online 6 July 2017)

The aim of this work is to better understand fluid displacement mechanisms at the pore scale in relation to capillary-filling rules. Using specifically designed micro-models we investigate the role of pore body shape on fluid displacement during drainage and imbibition via quasi-static and spontaneous experiments at ambient conditions. The experimental results are directly compared to lattice Boltzmann (LB) simulations. The critical pore-filling pressures for the quasi-static experiments agree well with those predicted by the Young–Laplace equation and follow the expected filling events. However, the spontaneous imbibition experimental results differ from those predicted by the Young–Laplace equation; instead of entering the narrowest available downstream throat the wetting phase enters an adjacent throat first. Thus, pore geometry plays a vital role as it becomes the main deciding factor in the displacement pathways. Current pore network models used to predict displacement at the field scale may need to be revised as they currently use the filling rules proposed by Lenormand *et al.* (*J. Fluid Mech.*, vol. 135, 1983, pp. 337–353). Energy balance arguments are particularly insightful in understanding the aspects affecting capillary-filling rules. Moreover, simulation results on spontaneous imbibition, in excellent agreement with theoretical predictions, reveal that the capillary number itself is not sufficient to characterise the two phase flow. The Ohnesorge number, which gives the relative importance of viscous forces over inertial and capillary forces, is required to fully describe the fluid flow, along with the viscosity ratio.

Key words: capillary flows, interfacial flows (free surface), porous media

1. Introduction

Understanding the fundamentals of fluid displacement processes in porous media is essential for multiple applications, from fluid uptake in diapers, humidity and fluid uptake in proton exchange membranes to carbon sequestration and enhanced

† Email address for correspondence: i.zacharoudiou@imperial.ac.uk

Downloaded from https://www.cambridge.org/core. Imperial College London Library, on 05 Sep 2017 at 14:28:43, subject to the Cambridge Core terms of use, available at https://www.cambridge.org/core/terms. https://doi.org/10.1017/jfm.2017.363

oil recovery. This involves understanding the dynamics of drainage and imbibition, which however is often hard to unravel due to the complexity of the porous medium in terms of pore geometry, surface roughness and wetting properties. Attempts to simplify the problem, in order to determine the fluid displacement pathways and the associated fluid distributions, have been carried out with pore network models (Blunt *et al.* 2002, 2013). Pore network models decompose the porous medium into an ensemble of geometric shapes and, based on the pioneering work of Lenormand, Zarcone & Sarr (1983), predict the fluid displacement at the field scale in a sequential manner. These models have been successful especially for the drainage case, but do not work so well for the imbibition case. Our aim in this paper is to demonstrate the importance of the pore geometry in determining the displacement pathways, especially for spontaneous imbibition, by studying the displacement dynamics in well-defined single capillaries and pore junctions.

A significant amount of work has been carried out on the subject of imbibition or capillary filling. A fluid penetrates a hydrophilic capillary due to the Laplace pressure across the fluid–fluid interface, or equivalently due to the decrease in the free energy of the system as the hydrophilic liquid wets the walls of the capillary. The system uses the energy liberated from wetting the walls to drive the fluid inside the capillary. Lucas (1918) and Washburn (1921) gave the first account of this phenomenon, but considered only the regime when all influences apart from the driving force and the viscous drag cease to exist. Still, their predictions could describe the experimentally observed time dependency of the filled length of the penetrating fluid, i.e. $l \sim sqrt(t)$. Several authors have further progressed the subject by considering effects not taken into account by Lucas and Washburn such as inertial (Quéré 1997; Diotallevi *et al.* 2009) and gravitational effects (Raiskinmäki *et al.* 2002), deviations from a Poiseuille velocity profile at the inlet of the capillary or at the interface (Levine *et al.* 1980; Dimitrov, Milchev & Binder 2007; Diotallevi *et al.* 2009) and variations of the dynamic contact angle (Quéré 1997; Pooley, Kusumaatmaja & Yeomans 2008). The effect of the solid surfaces on the imbibition process, whether this involves the roughness (Stukan *et al.* 2010) or patterned surfaces (Kusumaatmaja *et al.* 2008; Mognetti & Yeomans 2009) was also investigated. Finally, as the Lucas–Washburn regime is the asymptotic limit for long times, extensive work was devoted on the initial stages of capillary filling (Siegel 1961; Petrash, Nelson & Otto 1963; Dreyer, Delgado & Path 1994; Ichikawa & Satoda 1994; Quéré 1997; Zhmud, Tiberg & Hallstensson 2000; Zacharoudiou & Boek 2016).

In order to unravel the fundamentals of fluid displacement processes at the pore scale, experimental research with micro-models has been on-going for the past several decades. This has progressed considerably, from bead packs to complex networks representing rock thin sections (Chatenever & Calhoun Jr 1952; Lenormand *et al.* 1983; Hornbrook, Castanier & Pettit 1991; Giordano & Cheng 2001; Bico & Quéré 2003; Kavehpour, Ovryn & McKinley 2003; Rangel-German & Kovscek 2006; Kumar Gunda *et al.* 2011; Karadimitriou & Hassanizadeh 2012). Of particular interest are the displacement mechanisms controlling both primary drainage and imbibition processes (Lenormand *et al.* 1983; Yu & Wardlaw 1986; Lenormand 1990; Morrow & Mason 2001; Chang *et al.* 2009), especially with regards to capillary trapping during carbon sequestration (Chalbaud *et al.* 2007; Taku, Jessen & Orr 2007; Saadatpoor, Bryant & Sepehrnoori 2011; Tokunaga *et al.* 2013).

Lenormand *et al.* (1983) investigated these fluid displacement mechanisms in resin etched networks of straight throats varying in width, with multiple menisci displacement processes identified. In the case of two immiscible fluids (oil–air),

Downloaded from https://www.cambridge.org/core. Imperial College London Library, on 05 Sep 2017 at 14:28:43, subject to the Cambridge Core terms of use, available at https://www.cambridge.org/core/terms. https://doi.org/10.1017/jfm.2017.363

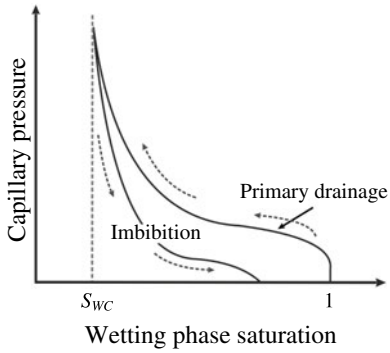

FIGURE 1. Schematic drainage/imbibition capillary pressure curve. During primary drainage the capillary pressure P_c systematically increases with increasing non-wetting phase saturation to connate water saturation (S_{WC}), whereas the capillary pressure decreases with increasing wetting phase saturation during imbibition.

Lenormand *et al.* (1983) illustrated that the Young–Laplace equation was sufficient to describe all menisci displacement mechanisms. The Young–Laplace equation (Rowlinson & Widom 1982) states

$$P_c = P_{nw} - P_w = \gamma \left(\frac{1}{r_1} + \frac{1}{r_2} \right), \tag{1.1}$$

where P_c is the capillary pressure, P_{nw} and P_w are the non-wetting phase (NWP) and wetting phase (WP) pressures respectively, γ is the surface tension and r_1, r_2 are the principal radii of curvature of the fluid interface. For throats with a rectangular cross-section this becomes $P_c = 2\gamma \cos\theta (1/d + 1/w_t)$, where θ is the contact angle and d, w_t are the depth and width of the throat. For primary drainage the porous medium is initially saturated with WP before NWP is forcibly injected, displacing the WP and thus causing the capillary pressure to systematically increase with increasing NWP saturation, see figure 1. Considering a pore junction with different throat widths, where the NWP enters from one of the throats, the Young–Laplace law (1.1) says that the NWP should select the downstream throat with the lowest capillary entry pressure first, i.e. by entering the widest throat. In the case of CO_2 sequestration in a saline aquifer, once injection of the NWP (CO_2) (Chiquet & Broseta 2007; Doughty, Freifeld & Trautz 2008; Hesse, Orr & Tchelepi 2008; Chalbaud *et al.* 2009) has stopped, the WP (brine) re-enters the porous medium via imbibition. During the imbibition process, the capillary pressure systematically decreases with increasing WP saturation, see figure 1. This means that, following (1.1), we expect that the WP will enter the narrowest downstream throat first, before sequentially filling all other throats in order of increasing diameter.

In reality, displacement processes are more complex as they are dependent on the pore geometry along with the WP and NWP location. In order to observe these displacement mechanisms experimentally, we used: (i) micro-fluidic devices as their transparent nature makes visualisation of fluid dynamics relatively simple and (ii) single pore geometries, rather than more complex networks, as single pore geometries allow us to accurately control the displacement processes in each throat individually; see figure 2 for schematic micro-model designs used. Furthermore, the models' characteristics, like pore geometry, surface energy and roughness, can be

Downloaded from https://www.cambridge.org/core. Imperial College London Library, on 05 Sep 2017 at 14:28:43, subject to the Cambridge Core terms of use, available at https://www.cambridge.org/core/terms. https://doi.org/10.1017/jfm.2017.363

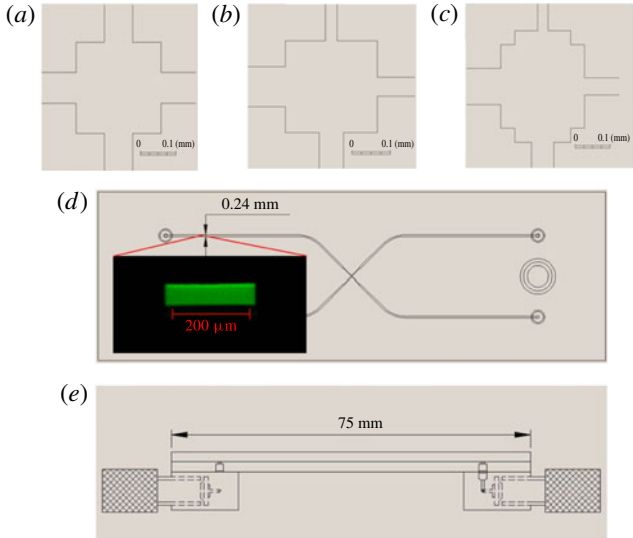

FIGURE 2. (Colour online) Schematic micro-model designs, including throat configuration and connectors. (*a*) Geometry 1: square pore with equal throats. (*b*) Geometry 2: square pore with unequal throats. (*c*) Geometry 3: pore with unequal throats. (*d*) Top down view of chip including confocal cross-section of a throat and (*e*) schematic cross-section of micro-model and connectors.

carefully controlled. The above enabled us to examine real-time primary drainage and imbibition events systematically via both quasi-static and spontaneous methods.

The quasi-static experiments are performed in a sequence of pressure steps, with hydrostatic equilibrium reached before progressing to the next pressure step. These quasi-static experiments are relevant to displacement processes occurring in the far field during CO_2 storage and enhanced oil recovery operations, associated with low Reynolds numbers. Displacement processes within pore network models (Øren, Bakke & Arntzen 1998; Øren & Bakke 2003; Valvatne & Blunt 2003; Sorbie & Skauge 2012) are performed in this fashion. The dynamic experiments were conducted as they are relevant to drainage and imbibition processes occurring near the well bore at relatively high Reynolds numbers. Further details on the experimental methods will be provided in the next section.

To further elucidate our experimental findings we compare experiments to lattice Boltzmann simulations in the same geometries. These provide the opportunity for a detailed investigation of the problem by varying the parameters under investigation over a wider range, not easily accessible to the experiments. The overall goal of this study is to challenge the pore-filling rules on which network models are based by comparing the sequence of throat filling in simple geometries for which the Laplace pressures can be calculated exactly and without ambiguity.

This paper is organised as follows; in the next section we provide the details of the experiments and the numerical scheme. We present and discuss our results in § 3. Finally conclusions drawn from this work are discussed in § 4.

Downloaded from https://www.cambridge.org/core. Imperial College London Library, on 05 Sep 2017 at 14:28:43, subject to the Cambridge Core terms of use, available at https://www.cambridge.org/core/terms. https://doi.org/10.1017/jfm.2017.363

2. Methodology

2.1. *Experimental section*

2.1.1. *Micro-fluidic models*

To conduct these experiments we had specifically designed micro-models fabricated in poly(methyl methacrylate) (PMMA), figure 2(*a–c*), by Epigem (Redcar). The fabrication procedure involves defining the pattern in the base layer of the model by using SU-8 (an epoxy based photoresist) via photolithography, which is achieved in two stages. Initially an under-layer is deposited (spin coated then dried) and fully cured before a secondary layer is deposited in the same way. The pattern is then created by exposing the coated models through a photo-mask and developing it to form the features. The top layer has a partially cured SU-8 layer deposited on the underside (this will form the top of the pattern) before the inlet/outlet holes are drilled into it. Finally, the base and top layer are assembled; figure 2(*e*) illustrates the cross-section of an assembled model. All the models have been chemically treated by Epigem, in order to increase the hydrophobicity of the surface. Additionally all models have an approximate etch depth of $d = 50$ μm. The designs are intended to explore pore geometry and the influence of varying throat diameters, providing a range of different capillary entry pressures.

2.1.2. *Experimental set-up*

All of the fluid displacement observations were captured via a high-speed video microscope (FastCam MC2.1, Photron) which is housed within a laminar flow cabinet (PurAir-48, Air Science). This is necessary due to the intricate nature of the micro-models, where unnecessary exposure to dust can lead to blockages rendering the micro-models unusable. Due to the hydrophobic nature of the micro-models, n-decane (viscosity $\eta_w = 0.85$ mPa s (Dymond & Øye 1994), surface tension $\gamma = 0.024$ N m^{-1} (Kuhn, Försterling & Waldeck 2009), density $\rho = 730$ kg m^{-3}, 99 %, Sigma-Aldrich) and air (viscosity $\eta_{nw} = 18.2$ μPa s, density $\rho = 1.2$ kg m^{-3}) were selected as the WP and NWP respectively. However, due to the unique fabrication of each micro-model, the etch depth/width and contact angle varied for each chip, with the contact angle always measured through the denser phase (Lyons 2009), resulting in different capillary entry pressures. All experiments were conducted at ambient conditions.

2.1.3. *Experimental procedure – primary drainage and imbibition*

The primary drainage experiments began with the models fully saturated with the WP. The NWP entered the model via either: (i) quasi-static displacement, achieved by gradually decreasing the WP pressure by siphoning the WP into a reservoir located below the model via the narrowest throat, or (ii) dynamic displacement – injection of the NWP at a constant flow rate of 0.5 μl min^{-1} via a programmable syringe pump (BS-8000, Braintree Scientific Ltd).

For imbibition the models were initially saturated with the NWP. During quasi-static displacement the model was connected to a reservoir of the WP and P_w was then gradually increased by raising the height of the reservoir. In contrast, spontaneous displacement was attained by placing a droplet of the WP over an inlet port which then spontaneously penetrated into the model.

2.2. *Numerical method*

In this section we describe the numerical method we shall use, starting with the thermodynamics in § 2.2.1, the dynamical equations of motion in § 2.2.2 and the lattice Boltzmann implementation in § 2.2.3.

Downloaded from https://www.cambridge.org/core. Imperial College London Library, on 05 Sep 2017 at 14:28:43, subject to the Cambridge Core terms of use, available at https://www.cambridge.org/core/terms. https://doi.org/10.1017/jfm.2017.363

2.2.1. *Thermodynamics of the fluid*

The equilibrium properties of a binary fluid can be described by a Landau free energy functional (Briant & Yeomans 2004)

$$\mathcal{F} = \int_V \left(f_b + \frac{\kappa_\phi}{2} (\partial_\alpha \phi)^2 \right) \mathrm{d}V + \int_S f_s \, \mathrm{d}S. \tag{2.1}$$

The first term in the integrand is the bulk free energy density given by

$$f_b = -\frac{A}{2}\phi^2 + \frac{A}{4}\phi^4 + \frac{c^2}{3}\rho \ln \rho, \tag{2.2}$$

where ϕ is the concentration or order parameter, ρ is the fluid mass density and c is a lattice velocity parameter. A is a constant with dimensions of energy per unit volume. This choice of f_b allows binary phase separation into two phases with bulk equilibrium solutions $\phi_{eq} = \pm 1$. The position of the interface is chosen to be the locus $\phi = 0$. The term in ρ controls the compressibility of the fluid (Kendon *et al.* 2001).

The presence of interfaces is accounted for by the gradient term $(\kappa_\phi/2)(\partial_\alpha \phi)^2$, which penalises spatial variations of the order parameter ϕ. This gives rise to the interface tension $\gamma = \sqrt{8\kappa_\phi A/9}$ and to the interface width $\xi = \sqrt{\kappa_\phi / A}$ (Briant & Yeomans 2004).

The final term in the free energy functional, equation (2.1), describes the interactions between the fluid and the solid surface. Following Cahn (1977), the surface energy density is taken to be of the form $f_s = -h\phi_s$, where ϕ_s is the value of the order parameter at the surface. Minimisation of the free energy gives an equilibrium wetting boundary condition (Briant & Yeomans 2004)

$$\kappa_\phi \partial_\perp \phi = -\frac{\mathrm{d}f_s}{\mathrm{d}\phi_s} = -h. \tag{2.3}$$

The value of the parameter h (the surface excess chemical potential) is related to the equilibrium contact angle θ^{eq} via (Briant & Yeomans 2004)

$$h = \sqrt{2\kappa_\phi A} \ \mathrm{sign} \ \left[\frac{\pi}{2} - \theta^{eq} \right] \sqrt{\cos\left(\frac{\alpha}{3}\right) \left\{ 1 - \cos\left(\frac{\alpha}{3}\right) \right\}}, \tag{2.4}$$

where $\alpha = \arccos(\sin^2 \theta^{eq})$ and the function sign returns the sign of its argument.

This choice of the free energy leads to the chemical potential

$$\mu = \frac{\delta \mathcal{F}}{\delta \phi} = -A\phi + A\phi^3 - \kappa_\phi \partial_{\gamma\gamma}\phi, \tag{2.5}$$

and the pressure tensor (Anderson, McFadden & Wheeler 1998)

$$P_{\alpha\beta} = \left[p_b - \kappa_\phi \phi \partial_{\gamma\gamma}\phi - \frac{\kappa_\phi}{2}(\partial_\gamma \phi)^2 \right] \delta_{\alpha\beta} + \kappa_\phi (\partial_\alpha \phi)(\partial_\beta \phi), \tag{2.6}$$

where $p_b = (c^2/3)\rho - (A\phi^2)/2 + (3/4)A\phi^4$ is the bulk pressure.

Downloaded from https://www.cambridge.org/core. Imperial College London Library, on 05 Sep 2017 at 14:28:43, subject to the Cambridge Core terms of use, available at https://www.cambridge.org/core/terms. https://doi.org/10.1017/jfm.2017.363

Downloaded from https://www.cambridge.org/core. Imperial College London Library, on 05 Sep 2017 at 14:28:43, subject to the Cambridge Core terms of use, available at https://www.cambridge.org/core/terms. https://doi.org/10.1017/jfm.2017.363

2.2.2. *Equations of motion*

The hydrodynamic equations for the system are the continuity, (2.7), and the Navier–Stokes, (2.8), equations for a non-ideal fluid

$$\partial_t \rho + \partial_\alpha(\rho u_\alpha) = 0, \tag{2.7}$$

$$\partial_t(\rho u_\alpha) + \partial_\beta(\rho u_\alpha u_\beta) = -\partial_\beta P_{\alpha\beta} + \partial_\beta[\eta(\partial_\beta u_\alpha + \partial_\alpha u_\beta)], \tag{2.8}$$

where $\boldsymbol{u}$, $\boldsymbol{P}$, η are the fluid velocity, pressure tensor and dynamic viscosity respectively. For a binary fluid the equations of motion are coupled with a convection–diffusion equation,

$$\partial_t \phi + \partial_\alpha(\phi u_\alpha) = M\nabla^2\mu, \tag{2.9}$$

that describes the dynamics of the order parameter ϕ. M is a mobility coefficient.

2.2.3. *Lattice Boltzmann method*

The equations of motion are solved using a standard free energy lattice Boltzmann algorithm for a binary fluid (Briant & Yeomans 2004). In particular we use a three-dimensional model with 19 discrete velocity vectors (D3Q19) and adopt a multiple relaxation time (MRT) (D'Humières *et al.* 2002) approach for the evolution of the distribution functions, f_i, associated with the fluid density ρ. Following Pooley, Kusumaatmaja & Yeomans (2009), the relaxation times responsible for generating the viscous terms in the Navier–Stokes equation are set to τ_f (based on the fluid viscosity $\eta = \rho(\tau_f - 0.5)/3$), those related to conserved quantities to infinity and all the others, which correspond to non-hydrodynamic modes, to unity. A single relaxation time approach is sufficient for the order parameter ϕ. The relaxation time for the evolution of the distribution functions, g_i, associated with the concentration ϕ is set to $\tau_g = 1$. As shown by Pooley *et al.* (2009), this approach suppresses spurious currents at the contact line, while improving significantly the numerical stability of the algorithm as well (Lallemand & Luo 2000). For a detailed description of the lattice Boltzmann (LB) implementation we refer the reader to (Briant & Yeomans 2004; Yeomans 2006; Pooley *et al.* 2008, 2009).

Numerically we solve the equations of motion using graphics processing units (NVIDIA Tesla K40 GPU cards), taking advantage of the fact that the LB method is particularly well suited for computations on a parallel architecture (Gray, Cen & Boek 2016). Running the simulations in parallel on 8 Tesla K40 cards reduces the required computational time to a few days for the most computationally intensive simulation.

3. Results and discussion

In this section we will present our results. We start with primary drainage, which also serves as a validation for our experiments. Then we turn our attention to the imbibition case, where we examine pore filling events and investigate the role of pore geometry in determining the displacement pathways.

3.1. *Primary drainage*

The model was initially filled with the WP. For the quasi-static displacement, the P_w was gradually decreased, allowing the NWP to enter the largest throat first, before sequentially displacing the WP from the throats in decreasing size order, as can be seen in figure 3. This type of displacement is referred to as 'piston-type' motion

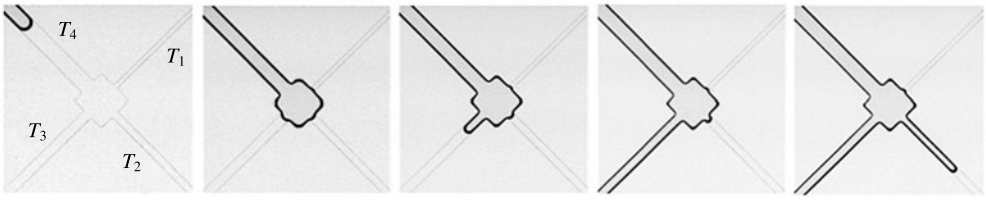

FIGURE 3. Quasi-static primary drainage images in a micro-model (Geometry 2) with etch depth $d = 45$ μm and throat widths w_t: 33, 51, 65, 107 μm (WP-white, NWP-grey). Contact angle 26°.

Throat	Young–Laplace equation	Young–Laplace Critical pressure (Pa)	Experimental pressure (Pa)
T_4	$P_p = 2\gamma \cos\theta^{eq}\left(\frac{1}{d} + \frac{1}{w_t}\right)$	1357	1361 ± 7
T_3	—	1620	1590 ± 7
T_2	—	1794	1790 ± 7

TABLE 1. Critical pressures for drainage in a micro-model (Geometry 2) with etch depth $d = 45$ μm and unequal throat widths w_t: 33, 51, 65 and 107 μm, calculated via (1.1) and experimental data. Contact angle: 26°, interfacial tension: 0.024 N m^{-1}. Experimental error of ±7 Pa is attained by the 1 mm accuracy the height of the reservoir can be set to.

(Lenormand *et al.* 1983), when the NWP enters the throat filled with the WP only if the capillary pressure is equal to or greater than a given value $P_p = P_{nw} - P_w = 2\gamma \cos\theta^{eq}(1/d + 1/w_t)$, which we call 'the critical pressure'. The calculated theoretical and experimental critical pressures for drainage within the throats are displayed in table 1. Generally there is good agreement between the two.

For the dynamic drainage, the NWP is injected into the chip at a constant flow rate of 0.5 μl min^{-1}. This leads to the displacement of the WP at a constant mean velocity u in each throat, prior to and after the square pore body. The corresponding capillary number for the interface motion in the throat prior to the pore body is $Ca = \eta_w u/\gamma \sim 10^{-4}$. Typical values for the ratio of viscous to capillary forces at the pore scale, quantified by the capillary number, are in the range of 10^{-3}–10^{-10}, depending on the distance from the injection point in the well bore (Blunt & Scher 1995). Again, as can be seen in figure 4(*a*), the NWP displaces the WP via the largest downstream throat first, as predicted by (1.1). To validate the displacement sequence, we have carried out LB simulations in exactly the same geometry, the same value for Ca and contact angle as in the experiment. The fluid flow was driven by applying velocity boundary conditions (Hecht & Harting 2010) at the inlet and outlet of the simulation domain to match the experimental conditions. The results are presented in figure 4(*b*) and display a good agreement with the experimental displacement sequence.

3.2. *Imbibition*

3.2.1. *Quasi-static imbibition*

Pore-filling events are dependent on the number of throats connected to the pore that are occupied with the NWP along with their orientation. Generally, pore-filling events are designated as I_1, I_2, I_3 ... I_n, with n indicating the number of throats

Downloaded from https://www.cambridge.org/core. Imperial College London Library, on 05 Sep 2017 at 14:28:43, subject to the Cambridge Core terms of use, available at https://www.cambridge.org/core/terms. https://doi.org/10.1017/jfm.2017.363

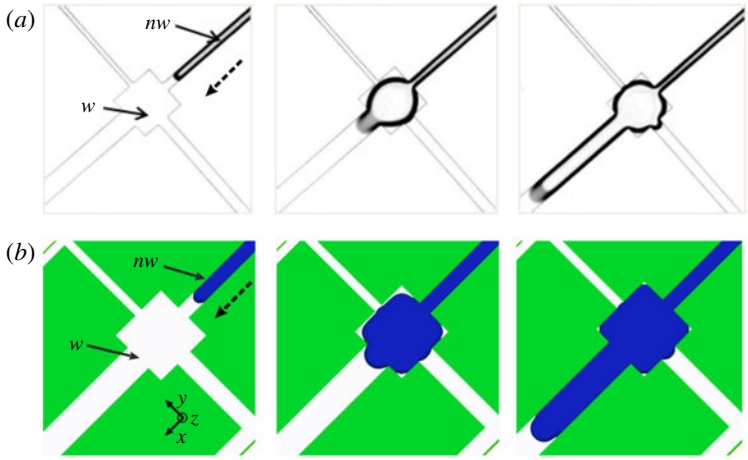

FIGURE 4. (Colour online) Primary dynamic drainage images: (*a*) experimental images of forced injection of NWP at 0.5 μl min^{-1}. (*b*) Corresponding LB simulations. The dashed arrow denotes the direction of the flow.

Pore-filling events	Young–Laplace for pore-filling event	Young–Laplace Critical pressure (Pa)	Experimental pressure (Pa)
I_1	$P_p = \gamma\left(\frac{2\cos\theta^{eq}}{d} + \frac{1}{r}\right)$	931	932 ± 7
I_2	—	838	838 ± 7
I_{2A}	—	745	754 ± 7
I_3	—	709	708 ± 7

TABLE 2. Critical pressures for each pore-filling event in a micro-model (Geometry 1) with equal throat widths. Contact angle: 28°, etch depth $d = 56$ μm, throat width $w_t = 73$ μm, pore width: 238 μm, interfacial tension: 0.024 N m^{-1}. The critical radii in the plane of the micro-model $r_2 = r$ used in the calculation of the critical pressures is shown in figure 5. The principal radii of curvature, equation (1.1), are $r_1 = d/2\cos\theta^{eq}$, $r_2 = r$. Experimental error of ±7 Pa is attained by the 1 mm accuracy the height of the reservoir can be set to.

filled with the NWP (Lenormand *et al.* 1983). Here $I_{1,2,2A,3}$ pore-filling events were investigated via quasi-static imbibition experiments, by gradually increasing P_w, in a micro-model with equal throat widths (Geometry 1: etch depth $d = 56$ μm, throat width $w_t = 73$ μm, pore width 238 μm), see figure 5. At a critical capillary pressure the WP spontaneously displaces the NWP via 'piston-type' displacement. In all cases the critical pressure of the pore-filling event calculated from the Young–Laplace equation is very close to the experimentally determined critical pressure, as shown in table 2. Good agreement is achieved as we know the exact pore geometry and can observe the meniscus shape, allowing the critical radii to be well defined, as illustrated for each case in figure 5.

Quasi-static experiments were also conducted in a micro-model (Geometry 3) with unequal throats (etch depth $d = 55$ μm, throat widths $w_t = 27$, 47, 60, 100 μm pore: 155, 236 μm). The predicted displacement sequence for this geometry,

Downloaded from https://www.cambridge.org/core. Imperial College London Library, on 05 Sep 2017 at 14:28:43, subject to the Cambridge Core terms of use, available at https://www.cambridge.org/core/terms. https://doi.org/10.1017/jfm.2017.363

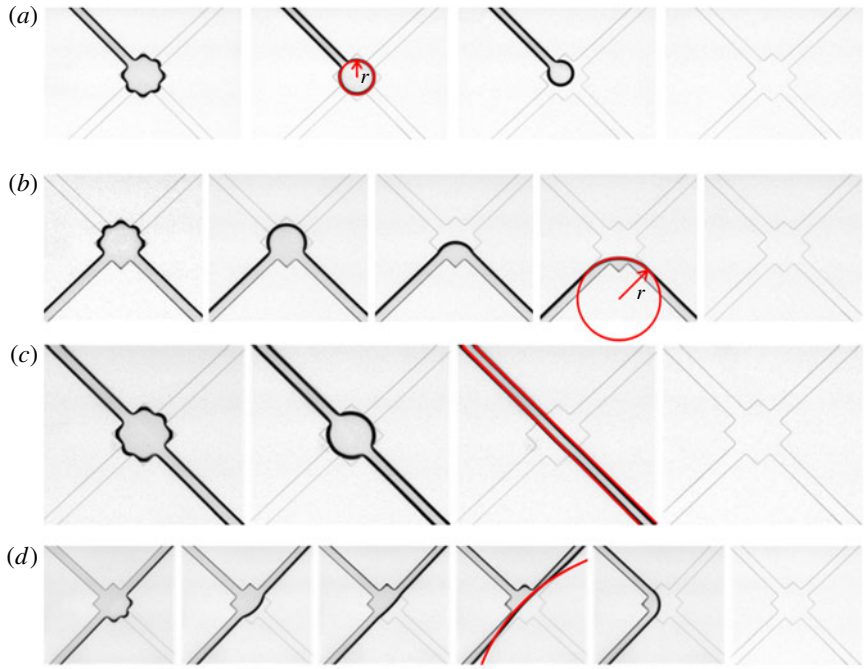

FIGURE 5. (Colour online) Quasi-static I_1, I_2, I_{2A} and I_3 imbibition experimental results (WP – white, NWP – grey). The critical radii in the plane of the micro-model, $r_2 = r$, used to calculate the displacement pressures for each case are also illustrated together with $r_1 = d/2 \cos \theta^{eq}$.

using the Young–Laplace equation and a contact angle of 16°, is first snap off (P_s) in the narrowest throat at 1240 Pa, followed by pore body filling via 'piston-type' displacement (P_p) at 869 Pa, see figure 6(*a*). The snap-off pressure, $P_s = 2\gamma(\cos \theta^{eq} - \sin \theta^{eq})/ \min(d, w_t)$, was estimated from the pressure at which two growing corner menisci meet on the channel wall (Valvatne & Blunt 2004). Snap off is able to occur during the quasi-static experiments, as there is time for the advancing WP films to develop ahead of the main meniscus, which swell and become unstable (Bico & Quéré 2003; Kavehpour *et al.* 2003), see figure 6(*b*), and because 'piston-type' displacement is not possible for topological reasons (Lenormand *et al.* 1983). The WP films can be clearly seen in figure 7 as the darker lines outlining the model geometry.

3.2.2. *Spontaneous imbibition*

Extending our research to spontaneous imbibition, we investigated the I_3 displacement mechanism, which was compared to LB simulations, figure 8. During our spontaneous imbibition experiments we observed that the advancing meniscus did travel down an adjacent throat (T_2) first instead of filling the smallest throat, as the WP films do not have time to develop ahead of the advancing meniscus. Indeed, Lenormand (1990) noted that when no wetting films are present along the corners of the models, the imbibing WP should enter an adjacent throat first, but no direct evidence was provided. Here we confirm this hypothesis directly and show our results in a series of snapshots from experiment and corresponding LB simulations in figure 8.

Downloaded from https://www.cambridge.org/core. Imperial College London Library, on 05 Sep 2017 at 14:28:43, subject to the Cambridge Core terms of use, available at https://www.cambridge.org/core/terms. https://doi.org/10.1017/jfm.2017.363

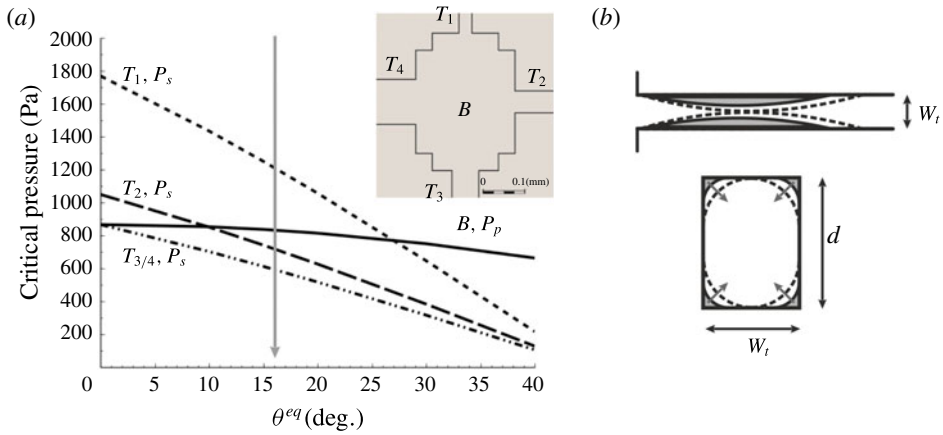

FIGURE 6. (*a*) Predicted displacement sequence for quasi-static I_3 imbibition (Geometry 3) using the Young–Laplace equation for a contact angle of 16°, with the narrowest throat filling first via snap off (P_s), followed by the body filling through piston-like displacement (P_p). (*b*) Schematic illustration of the snap-off mechanism. Swelling of the corner WP films leads to snap off when the menisci meet on the channel wall (dashed line) and become unstable. Top panel: configuration in the plane of the micro-model at the channel wall. Bottom panel: cross-sectional view in the orthogonal plane.

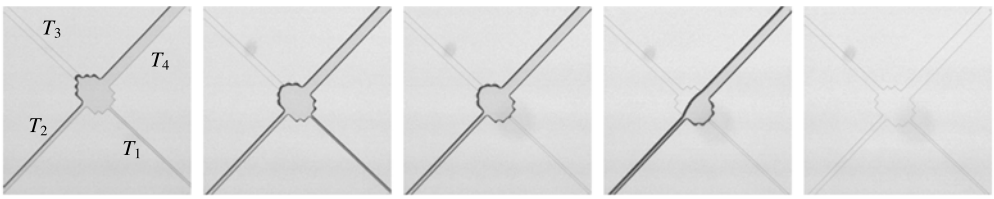

FIGURE 7. Quasi-static I_3 imbibition experimental results (WP – white, NWP – grey, wetting films – black). Snap off occurs in the narrowest throat before the meniscus enters the pore as predicted by the Young–Laplace equation.

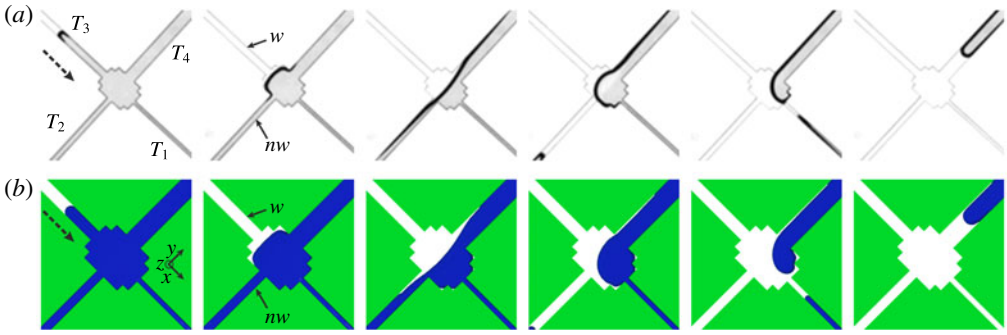

FIGURE 8. (Colour online) Spontaneous I_3 imbibition experimental results ((*a*), Geometry 3, throat widths: $(T_1)w_t = 27$ μm, $(T_2)w_t = 47$ μm, $(T_3)w_t = 60$ μm, $(T_4)w_t = 100$ μm, etch depth $d = 55$ μm), with the corresponding LB simulations (*b*); here the WP travels down the adjacent throat first. This behaviour is not predicted by the Young–Laplace law (1.1). Equilibrium contact angle $\theta^{eq} = 16°$, viscosity ratio $r_\eta = \eta_w/\eta_{nw} = 50$.

Downloaded from https://www.cambridge.org/core. Imperial College London Library, on 05 Sep 2017 at 14:28:43, subject to the Cambridge Core terms of use, available at https://www.cambridge.org/core/terms. https://doi.org/10.1017/jfm.2017.363

Thus, displacement does not occur in the order predicted by the Young–Laplace equation. This is understandable as all the downstream throats have lower critical entry pressures than the pore body. Therefore, as soon as the critical pore-filling pressure has been exceeded, the WP can enter any of the downstream throats. Hence, in the case of spontaneous imbibition, the pore body geometry becomes a key factor in determining in which order the downstream throats will fill.

Capillary-filling dynamics in a rectangular throat

A reasonable assumption then could be that the dynamics of imbibition in the throat prior to the junction (T_3) may affect the pore filling sequence and the selection of the displacement pathway. Hence, we turn our attention to the imbibition dynamics. We recently (Zacharoudiou & Boek 2016) examined the dynamics of capillary filling in two-dimensional channels and covered both: (i) the limit of long times for both high and low viscosity ratios $r_\eta = \eta_w/\eta_{nw}$ and (ii) the limit of short times, demonstrating that the free energy LB method can capture the correct dynamics for the process. We recall that in the limit of high viscosity ratios and long times, when the total time is much larger than the viscous time scale $t_v \sim \rho L_s^2/\eta_w$ (Quéré 1997; Stange, Dreyer & Rath 2003), the Lucas–Washburn regime ($l \sim sqrt(t)$) (Lucas 1918; Washburn 1921) is expected. In the limit of short times two regimes, namely (i) inertial regime ($l \sim t^2$) and (ii) visco–inertial regime ($l \sim t$) can precede the Lucas–Washburn regime (Dreyer *et al.* 1994; Stange *et al.* 2003). The hydraulic diameter $D_h = 2dw_t/(d + w_t)$ is used as the characteristic length scale L_s for evaluating t_v.

Ichikawa, Hosokawa & Maeda (2004) examined the interface motion driven by capillary action in the case of three-dimensional channels with a rectangular cross-section. Using the analytical solution of Brody, Yager & Austin (1996) for the velocity profile in a rectangular channel of aspect ratio $\epsilon = d/w_t$ and balancing the relevant forces, they estimated the dimensionless relation for the interface position as a function of time

$$l^{*2} = \cos\theta^{eq}(t^* - 1 + \mathrm{e}^{-t^*}). \tag{3.1}$$

The rescaled time and length are defined as $t^* = t/t_c$ and $l^* = l/l_c$ respectively, where

$$t_c = \frac{8\epsilon^2\left[1 - \dfrac{2\epsilon}{\pi}\tanh\left(\dfrac{\pi}{2\epsilon}\right)\right]}{\pi^4} \times t_v, \quad l_c = 2t_c\sqrt{\frac{(1+\epsilon)\gamma}{\epsilon\rho w_t}}. \tag{3.2a,b}$$

Here, we first compare our results with the theoretical prediction of Ichikawa *et al.* (2004), equation (3.1), before examining whether the capillary-filling dynamics affects the displacement pathway after the junction. We considered equilibrium contact angles of $\theta^{eq} = 30°$ and $16°$ (experimental condition). Starting with a situation with a high viscosity ratio $r_\eta = \eta_w/\eta_{nw} = 500$ by choosing relaxation rates $\tau_{f,w} = 1.5$ and $\tau_{f,nw} = 0.502$, we decrease the viscosity ratio to $r_\eta = 5$ by decreasing η_w, while η_{nw} is kept fixed. This choice decreases the rate of viscous dissipation in the WP as the viscosity ratio decreases from $r_\eta = 500$ to $r_\eta = 5$, allowing for more energy to be available to the interface motion as it enters the junction region.

Figure 9(*a*) shows the length of the penetrating WP column in throat T_3 for simulations with varying viscosity ratio r_η and $\theta^{eq} = 30°$. In the limit of long times and high viscosity ratios the Lucas–Washburn regime ($l \sim sqrt(t)$) (Lucas 1918; Washburn 1921) is clearly observed. The viscous time scale t_v is of the order of 10^4 in lattice units (l.u.) for $r_\eta = 25$, 50, thus enabling us to also obtain the $l \sim t^2$

Downloaded from https://www.cambridge.org/core. Imperial College London Library, on 05 Sep 2017 at 14:28:43, subject to the Cambridge Core terms of use, available at https://www.cambridge.org/core/terms. https://doi.org/10.1017/jfm.2017.363

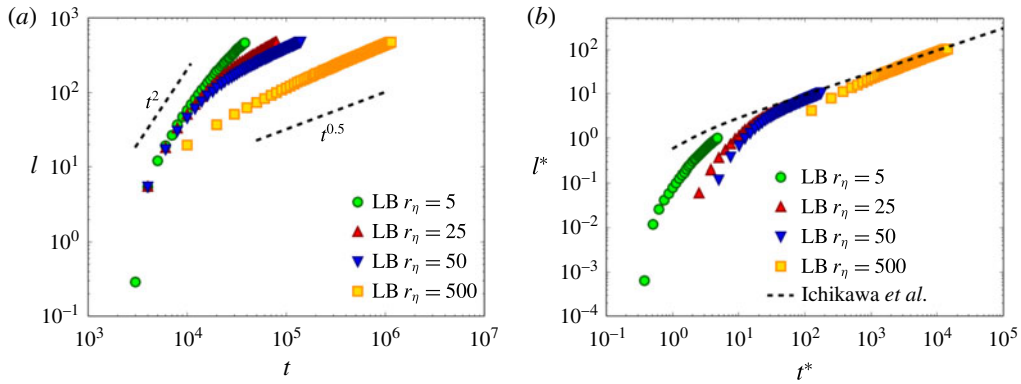

FIGURE 9. (Colour online) (*a*) Length of the penetrating fluid column in throat T_3 for simulations with varying viscosity ratio $r_\eta = \eta_w/\eta_{nw}$ as a function of time in lattice units (l.u.). What appears as a deviation from the $l \sim t^2$ regime at early times (first point for $r_\eta = 5$) is due to the interface retracting initially in the connected reservoir which can result in interfacial oscillations (Stange *et al.* 2003; Zacharoudiou & Boek 2016). (*b*) Length versus time in scaled units according to (3.2). The theoretical prediction of Ichikawa *et al.* (2004), equation (3.1), is given with the dashed line.

regime at early times, as the interface accelerates initially penetrating the throat. This initial acceleration of the interface for $r_\eta = 5$, 25 and 50 is reflected in the increasing dynamic contact angle θ^α_{xz}, shown in figure 10(*a*).

Rescaling length and time using (3.2) reveals that our numerical results approach the theoretical prediction of Ichikawa *et al.* (2004), equation (3.1), in the limit of long times as shown in figure 9(*b*). Here we used the equilibrium value of the contact angle $\theta^{eq} = 30°$, although actually the dynamic contact angle, shown in figure 10(*a*), varies with time as it depends on the interfacial velocity and Ca (Cox 1986; Sheng & Zhou 1992). Using the dynamic contact angle instead would decrease slightly l^* improving the agreement further. The dynamic contact angle, in the xy and xz planes, is evaluated by fitting the interface in the central region of the advancing meniscus to a circle, as shown in figure 10(*c*). The angle of intersection this circle makes with the side walls is $\theta^\alpha_{xy,xz}$.

Figure 10(*b*) depicts the variation of $\cos(\theta^\alpha_{xz})$ as a function of the capillary number Ca. This is in agreement with the theoretical predicted dependency of θ^α_{xz} on Ca (Cox 1986; Sheng & Zhou 1992)

$$\cos\theta^\alpha = \cos\theta^{eq} - Ca\ln(KL_s/l_s). \tag{3.3}$$

K is a fitting constant, L_s is a characteristic length scale of the system and l_s is the effective slip length at the contact line. High interfacial velocities translate to high θ^α_{xz}, while as the interface slows down θ^α_{xz} approaches the equilibrium value θ^{eq}. Fitting the results for each simulation set to (3.3) and extrapolating to $Ca = 0$ reveals the following $\theta^\alpha_{Ca=0} = 29.2°$, 30.3°, 30.9° and 29.4° for $r_\eta = 5$, 25, 50 and 500 respectively. Hence, this verifies that the dynamic contact angle tends to the correct value for the equilibrium contact angle of $\theta^{eq} = 30°$. The deviation increases for the case of $\theta^{eq} = 16°$ and is of the order of a few degrees ($\sim 5°$). This is expected for very small or large contact angles due to the finite width of the interface and has been observed

Downloaded from https://www.cambridge.org/core. Imperial College London Library, on 05 Sep 2017 at 14:28:43, subject to the Cambridge Core terms of use, available at https://www.cambridge.org/core/terms. https://doi.org/10.1017/jfm.2017.363

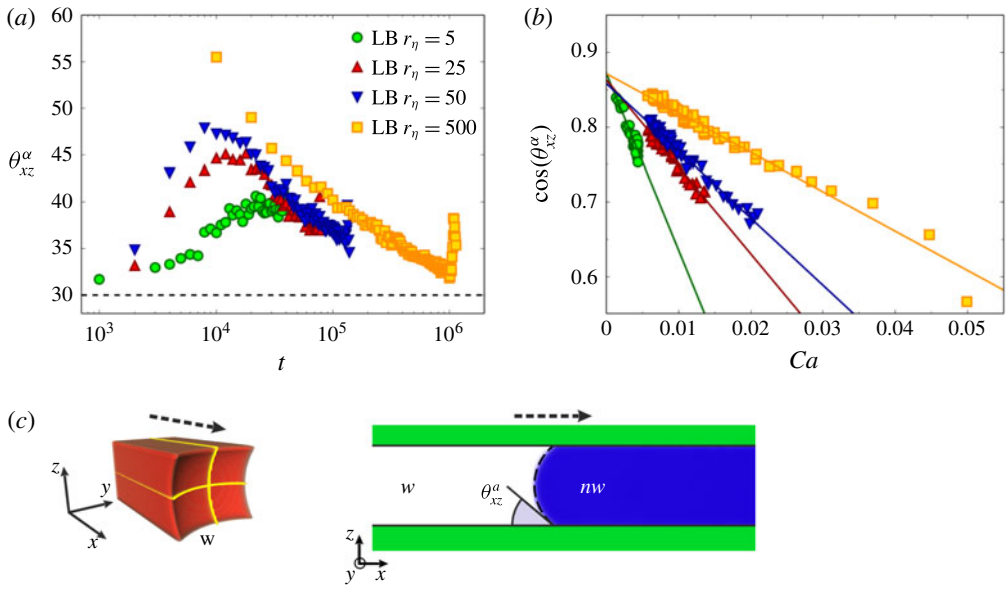

FIGURE 10. (Colour online) (*a*) Time variation of the dynamic contact angle in the xz plane (etch depth direction) θ^α_{xz} for the imbibition process in throat T_3. The behaviour of θ^α_{xy} is the same. The increase observed in θ^α_{xz} at the end of each simulation set is due to the interface reaching the end of throat T_3 and entering the junction region. The equilibrium value of the contact angle $\theta^{eq} = 30°$ (dashed line). (*b*) The cosine of θ^α_{xz} plotted against the capillary number Ca. Results affected by the interface approaching the junction region were excluded. The solid lines correspond to linear fits of each data set to Ca to enable comparison with the theoretical prediction of Cox (1986), Sheng & Zhou (1992), equation (3.3). (*c*) Illustration of the WP column configuration, as it imbibes throat T_3, and the definition for the dynamic contact angle.

for binary and ternary systems as well (Pooley *et al.* 2009; Semprebon, Krüger & Kusumaatmaja 2016).

We next examined the velocity of the interface front. Decreasing the viscosity ratio by decreasing the viscosity of the WP results in less viscous dissipation in the WP and hence more energy becomes available for driving the interface in the channel. Figure 11(*a*) shows the corresponding $Ca = \eta_w u/\gamma$. The experimental Ca is of the order of 10^{-2} ($r_\eta \sim 50$). Ichikawa *et al.* (2004) estimated the dimensionless velocity

$$u^* = \frac{\mathrm{d}l^*}{\mathrm{d}t^*} = \frac{1}{2}\sqrt{\frac{\epsilon \rho w_t}{(1+\epsilon)\gamma}}\,u, \tag{3.4}$$

which, in the limit of long times, approaches

$$u^* = \frac{1}{2}\sqrt{\frac{\cos\theta^{eq}}{t^*}}. \tag{3.5}$$

Although they neglected variations in the advancing dynamic contact angle θ^α, equation (3.5) can still be considered valid in the limit of long times as the advancing contact angle θ^α approaches the equilibrium value θ^{eq}. It is evident that the numerical results demonstrate excellent agreement with the theoretical prediction of Ichikawa *et al.* (2004) (figure 11*b*).

Downloaded from https://www.cambridge.org/core. Imperial College London Library, on 05 Sep 2017 at 14:28:43, subject to the Cambridge Core terms of use, available at https://www.cambridge.org/core/terms. https://doi.org/10.1017/jfm.2017.363

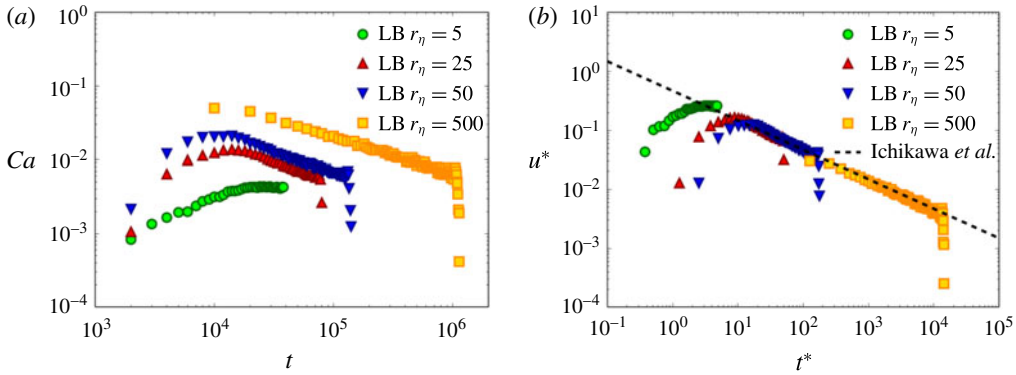

FIGURE 11. (Colour online) (*a*) The capillary number, $Ca = \eta_w u/\gamma$, for the interface front motion in throat T_3 as a function of time (in l.u.) for varying r_η and $\theta^{eq} = 30°$. At the end of throat T_3 the velocity decreases significantly, as the interface enters the junction region. (*b*) Interfacial velocity and time in scaled units. The theoretical prediction of Ichikawa *et al.* (2004), equation (3.5), is given with the dashed line.

Junction region

Having validated the interface motion in the throat prior to the junction, we next examine the interface motion in the wider pore body. As the interface approaches the end of throat T_3 and enters the junction region, it decelerates at first as the driving capillary forces per unit area decrease and the interface adapts a concave shape in the *xy*-plane. This reduction in the interfacial velocity is evident in figure 11. On the other hand inertial forces can keep the interface moving in the junction, while the motion is opposed by viscous forces that can damp this forward movement. Hence, an important dimensionless number that can affect the dynamics of the interface entering the junction is the Ohnesorge number

$$Oh = \frac{\eta_w}{\sqrt{\rho \gamma L_s}}, \tag{3.6}$$

which gives the relative importance of viscous forces over inertial and capillary forces. Inertial forces (per unit volume), which scale as $\sim \rho u^2/L_s$, are in the range 10^{-6} ($r_\eta = 5$)–10^{-9} ($r_\eta = 500$) in l.u. Viscous forces (per unit volume), which scale as $\sim \eta_w u/L_s^2$, are in the range 10^{-8} in l.u. for all cases as r_η increases from 5 to 500. Capillary forces $F_{cap} = 2\gamma \cos\theta^\alpha (d + w_t)$ are of the order of 1 in l.u. for all cases.

On a second stage, the contact line in the *xy*-plane makes contact with the side walls, see figure 12(*a*). As this favours energetically a transition from a concave to a convex configuration (dashed yellow line to the solid black line configuration), the surface energy released and the interface configuration transition can lead to interfacial oscillations, which, as demonstrated in figure 12(*b*), are more profound with decreasing *Oh*. Time is normalised by the time t_{cont} when the interface imbibes throat T_2. Similar interfacial oscillations have been observed by Ferrari & Lunati (2013), who examined a forced imbibition situation. Here we demonstrate that these oscillations can be generated as the interface travels through a narrow throat to a wider pore body in a spontaneous imbibition scenario as well, due to the small *Oh*, with the mechanism behind this being the same. As the interface progresses further in the junction, the kinetic energy that was available is gradually dissipated and the

Downloaded from https://www.cambridge.org/core. Imperial College London Library, on 05 Sep 2017 at 14:28:43, subject to the Cambridge Core terms of use, available at https://www.cambridge.org/core/terms. https://doi.org/10.1017/jfm.2017.363

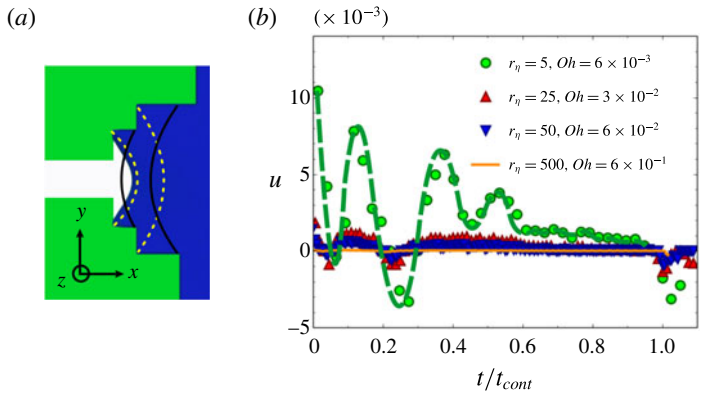

FIGURE 12. (Colour online) (*a*) Interface configuration in the *xy*-plane at $z = d/2$ as the interface enters the junction region. When the contact line makes contact with the side walls the interface configuration can change from concave to convex leading to interfacial oscillations. (*b*) Velocity of the interface (in l.u.) measured along the dashed line shown in figure 13 for simulations with varying r_η and Ohnesorge number (Oh). Interfacial oscillations are evident, especially as Oh decreases. Results are plotted as a function of dimensionless time $t^* = t/t_{cont}$, where time is normalised by the time t_{cont} when the interface imbibes throat T_2.

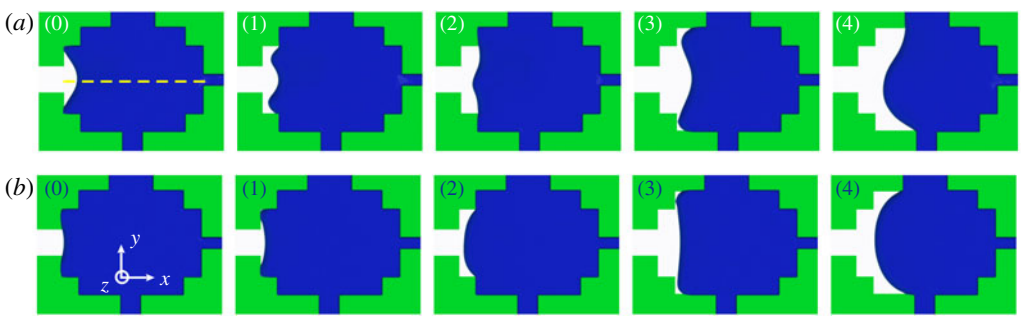

FIGURE 13. (Colour online) Interface configuration in the *xy*-plane ($z = d/2$) in the junction for (*a*) $r_\eta = 5$, $Oh = 6 \times 10^{-3}$ and (*b*) $r_\eta = 50$, $Oh = 6 \times 10^{-2}$.

forward movement is due to the action of capillary filling. This becomes more clear when looking at the interface configuration in the junction at a level $z = d/2$ for viscosity ratios $r_\eta = 5$ ($Oh = 6 \times 10^{-3}$) and $r_\eta = 50$ ($Oh = 6 \times 10^{-2}$), figure 13.

Figure 14(*a*) shows the length travelled by the meniscus in the junction, measured along the dashed line in figure 13, for varying r_η and Oh. The similar shape of the curves, with two peaks – labelled as (1) and (3) – and two troughs – points (2) and (4) – is due to the transition from a concave to convex configuration, favoured by the shape of the junction. As expected, increasing the viscosity of the wetting phase (increasing r_η) increases the time it takes for the interface to imbibe into the next downstream throat, t_{cont}. For all situations examined here, the fluid imbibes throat T_2 first, which is achieved when the interface has progressed a length $l \sim 85$ in the junction region. In other words, geometry dictates the pore-filling sequence, irrespective of the dynamics prior to the selection of the next downstream throat or the filling rules proposed by Lenormand *et al.* (1983). The same is observed

Downloaded from https://www.cambridge.org/core. Imperial College London Library, on 05 Sep 2017 at 14:28:43, subject to the Cambridge Core terms of use, available at https://www.cambridge.org/core/terms. https://doi.org/10.1017/jfm.2017.363

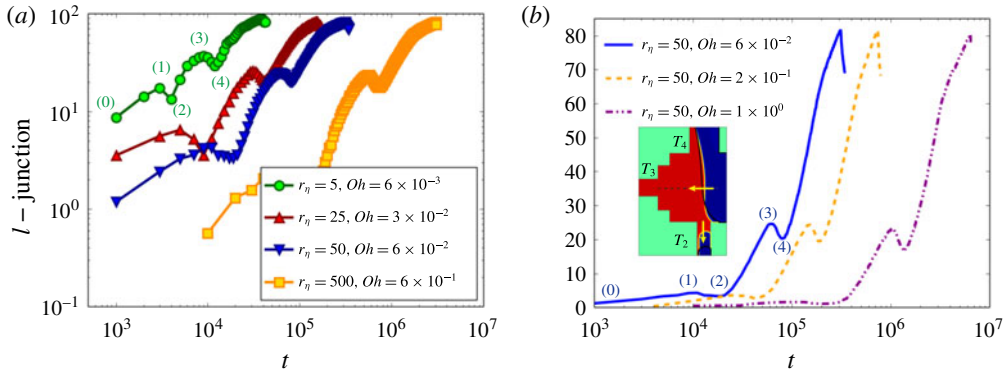

FIGURE 14. (Colour online) Junction region: (*a*) length versus time (in l.u.) for varying viscosity ratios r_η, measured along the line shown in figure 13(*a*). The wetting fluid starts imbibing the next downstream throat (T_2) when $l \sim 85$ and $t = t_{cont}$. (*b*) Simulation results with $r_\eta = 50$ and different Oh, by varying the viscosities of both phases. Increasing fluids' viscosities increases Oh and t_{cont}. The average $Ca = \eta_w \bar{u}/\gamma$ for the interface motion in the junction is 8.1×10^{-4} ($Oh = 6 \times 10^{-2}$), 8.4×10^{-4} ($Oh = 2 \times 10^{-1}$) and 7.9×10^{-4} ($Oh = 1 \times 10^{0}$). The labels (0)–(4) correspond to the snapshots in figure 13(*b*). Inset: the moment the wetting phase starts imbibing the throat T_2 ($t = t_{cont}$) the interface retracts in the middle of the junction (reduction in l).

for the simulations reported in figure 14(*b*), which examines simulations with the same viscosity ratio ($r_\eta = 50$) and different Oh, achieved by varying the viscosity of both phases. We note here that the capillary number is approximately the same in these simulations ($Ca \sim 8 \times 10^{-4}$); t_{cont} varies significantly though as can be clearly observed, as a consequence of the different rates at which energy is dissipated in the system. Therefore, an important remark here is that Ca itself is not sufficient to characterise the fluid flow. The dimensionless numbers, relevant to the specific type of fluid flow, must be matched, for example the viscosity ratio r_η and the Oh, in order to characterise the fluid flow dynamics.

Examining the imbibition process in the junction in terms of the surface energies, and given that we kept all parameters fixed except for the fluid viscosities, we note that the surface energy released, due to wetting, and used to drive the fluid–fluid interface, is the same for all runs. What changes is the rate of viscous dissipation,

$$\Phi = 2 \int_V \eta_i \dot{\epsilon}_{\alpha\beta} \dot{\epsilon}_{\alpha\beta} \, \mathrm{d}V > 0, \tag{3.7}$$

which dictates how much energy is left available as kinetic energy for the fluid motion. η_i ($i = w, nw$) is the local viscosity and $\dot{\epsilon}_{\alpha\beta} = (\partial_\alpha u_\beta + \partial_\beta u_\alpha)/2$ is the rate of strain tensor. For the spontaneous imbibition situation we examine here, the energy balance states (Ferrari & Lunati 2013)

$$\frac{\mathrm{d}E_k}{\mathrm{d}t} = -\frac{\mathrm{d}F}{\mathrm{d}t} - \Phi, \tag{3.8}$$

where E_k and F are the kinetic energy and surface free energy respectively. In figure 15(*a*) the viscous dissipation rate is plotted as a function of time for two of the simulations reported in figure 14(*b*), covering the interface motion both in throat

Downloaded from https://www.cambridge.org/core. Imperial College London Library, on 05 Sep 2017 at 14:28:43, subject to the Cambridge Core terms of use, available at https://www.cambridge.org/core/terms. https://doi.org/10.1017/jfm.2017.363

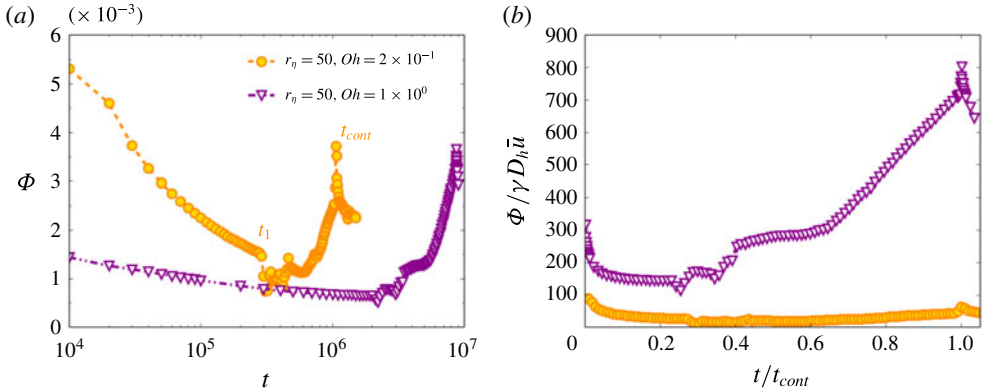

FIGURE 15. (Colour online) (*a*) Viscous dissipation rate as a function of time (in l.u.) for the simulations reported in figure 14(*b*). This covers the fluid–fluid interface motion in the throat T_3 ($t \leqslant t_1$) and in the junction region ($t \geqslant t_1$). The corresponding values of viscosities are $\eta_w = 8.33 \times 10^{-2}$, $\eta_{nw} = 1.67 \times 10^{-3}$ ($Oh = 2 \times 10^{-1}$) and $\eta_w = 6.67 \times 10^{-1}$, $\eta_{nw} = 1.33 \times 10^{-2}$ ($Oh = 1 \times 10^{0}$). (*b*) Viscous dissipation rate versus time in scaled units.

T_3 (prior the junction) and in the junction region. In figure 15(*b*) viscous dissipation rate in dimensionless form $\Phi^* = \Phi/\gamma D_h \bar{u}$ is plotted as a function of dimensionless time $t^* = t/t_{cont}$. As the viscosity of both fluids increases to maintain the same r_η, the total amount of energy dissipated (area under the curves, i.e. $\int \Phi \, \mathrm{d}t$) increases, and hence the change in kinetic energy decreases. The peak which is clearly visible for each case, corresponds to time $t = t_{cont}$, when the wetting fluid starts imbibing throat T_2, resulting in an increase in the fluid velocity.

The change in the total surface energy can be expressed as

$$\mathrm{d}F = \gamma \, \mathrm{d}A_{int} + \gamma_{ws} \, \mathrm{d}A_{ws} + \gamma_{ns} \, \mathrm{d}A_{ns}, \tag{3.9}$$

where $\mathrm{d}A_{int}$, $\mathrm{d}A_{ws}$ and $\mathrm{d}A_{ns}$ are the increments of the areas of the fluid–fluid, solid–wetting phase fluid and solid–non-wetting phase fluid interfaces respectively and γ, γ_{ws}, γ_{ns} the corresponding surface tensions. Given that the total solid surface area $A^s_{tot} = A_{ns} + A_{ws}$ is constant and that $\mathrm{d}A_{ns} = -\mathrm{d}A_{ws}$, then

$$\mathrm{d}F = \gamma (\mathrm{d}A_{int} - \cos\theta^{eq} \, \mathrm{d}A_{ws}). \tag{3.10}$$

The total surface energy is given by $F = \gamma(A_{int} - \cos\theta^{eq} A_{ws}) + F_0$, where $F_0 = \gamma_{ns} A^s_{tot}$ is constant. Plotting $F - F_0$ as a function of dimensionless time $t^* = t/t_{cont}$ in figure 16(*a*), reveals that the total surface energy decreases monotonically. It also demonstrates that the released energy is approximately the same for all simulations, as expected.

Finally, an interesting feature was observed when comparing situations with the same viscosity ratio ($r_\eta = 50$), see figure 14(*b*). The longer times t_{cont} observed, as viscous dissipation (and Oh) increases, allow more time to the interface to progress along the corners of the side throats. This is shown in figure 16(*b*), where we plot the area of the fluid–fluid interface as well as in figure 17, where we show snapshots of the interface configuration in the junction. In a complex geometry, as in porous media, swelling of these films and the consequent collapse can affect the displacement pathways. Especially in porous media and natural rock formations the

Downloaded from https://www.cambridge.org/core. Imperial College London Library, on 05 Sep 2017 at 14:28:43, subject to the Cambridge Core terms of use, available at https://www.cambridge.org/core/terms. https://doi.org/10.1017/jfm.2017.363

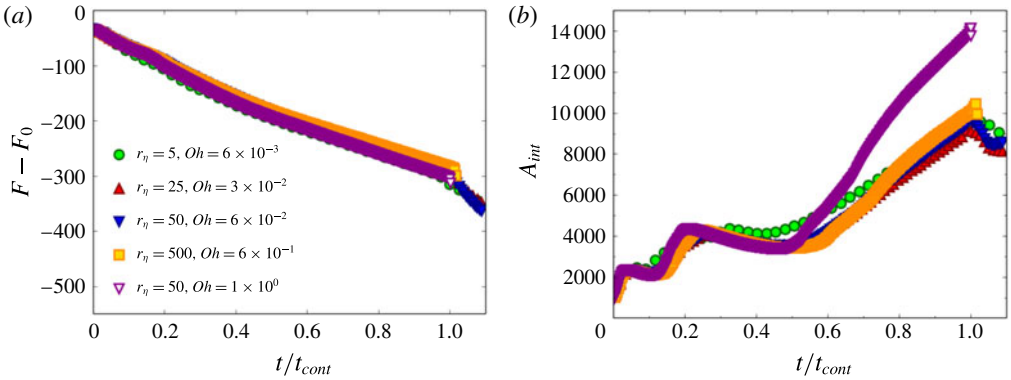

FIGURE 16. (Colour online) (*a*) The total surface energy $F - F_0$ (in l.u.) as a function of dimensionless time $t^* = t/t_{cont}$ in the junction region for varying viscosity ratios r_η. The energy released from wetting the solid surfaces ($\mathrm{d}F < 0$) drives the fluid inside the micro-model geometry. (*b*) The area of the fluid–fluid interface (in l.u.). This is measured using the marching cubes algorithm.

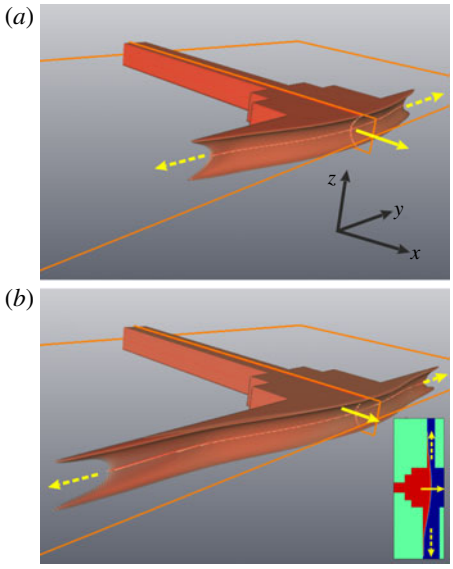

FIGURE 17. (Colour online) Wetting film growth in the side throats, along the dashed lines, for the simulations reported in figures 14(*b*) and 15 with $r_\eta = 50$ and (*a*) $Oh = 2 \times 10^{-1}$, (*b*) $Oh = 1 \times 10^{0}$. A situation with higher viscous dissipation rate (*b*) decreases the amount of energy converted to kinetic energy and hence the mean velocity along the x-direction. This gives more time for the development of thin wetting films progressing along the corners of the micro-channel. The snapshots correspond at the same length travelled in the x-direction and approximately at the same normalised time $t^* = t/t_{cont}$.

effective diameter varies continuously with length, favouring filling of the narrowest downstream throat as predicted by the filling rules of Lenormand *et al.* (1983). Here, however, and examining a wide range of parameters relevant to spontaneous

Downloaded from https://www.cambridge.org/core. Imperial College London Library, on 05 Sep 2017 at 14:28:43, subject to the Cambridge Core terms of use, available at https://www.cambridge.org/core/terms. https://doi.org/10.1017/jfm.2017.363

imbibition dynamics, LB simulations revealed that the pore-filling sequence remained the same, with the pore geometry being the major influencing factor.

4. Conclusions

It was observed that for both the drainage and quasi-static imbibition experiments the displacement pathways predicted by the Young–Laplace law are obeyed. LB simulations also followed these displacement predictions for drainage. In addition, the theoretical critical pressures for displacement events were in good agreement with calculated experimental events. For our spontaneous imbibition experiments, on the other hand, we found that the WP enters an adjacent throat first due to the absence of WP film growth. Lenormand (1990) suggested that the imbibing WP should enter an adjacent throat first, but no direct evidence was provided. Here we confirm this hypothesis, for the first time, directly using experiment and corresponding LB simulations. Thus, pore geometry plays a vital role as it becomes the main deciding factor in the displacement pathways. Once the critical pressure of the pore has been exceeded, all downstream throats are able to be filled. This displacement choice was observed in both our spontaneous imbibition experiments, and the corresponding LB simulations for models of the same geometry. The implications of the absence of WP films within the models have not been investigated.

Furthermore, we observe that the displacement of the meniscus in a throat and the scaling of the imbibing fluid column with time can fall in the early time flow regimes of capillary filling ((i) $l \sim t^2$, (ii) $l \sim t$) prior the Lucas–Washburn regime ((iii) $l \sim sqrt(t)$). An in-depth investigation of imbibition dynamics using lattice Boltzmann simulations was carried out in Zacharoudiou & Boek (2016). We emphasise here that matching the relevant dimensionless numbers is essential in correctly resolving the multiphase flow dynamics, as Ca itself is not sufficient to uniquely describe the flow. For example, we need to match the viscosity ratio and the Ohnesorge number, which for fluid flow at the pore scale is typically $Oh \ll 1$. Nevertheless, for the range of parameters examined here, LB simulations revealed that the pore-filling sequence remained the same. Therefore, the main message of the current paper is that the filling order of channels connected to a junction depends primarily on the geometry of the pore body and is largely independent of the details of the dynamic meniscus shape influenced by inertial effects.

In addition to the above, in real porous media, microscopic WP films can develop under strong wetting conditions and flow through the cervices and the micro-roughness of the pore walls, whereas in our micro-fluidic devices WP films develop at the right-angled wedges. This, however, will not change the main message of the current paper. Several papers in the literature have discussed the development of thin WP films in porous media, including Vizika, Avraam & Payatakes (1994), Constantinides & Payatakes (2000), Bico & Quéré (2003). Depending on the time scales associated with the general advancement of the fluid–fluid interface (t_{adv}) and the time scales for thin films to develop and swell (t_{film}), the displacement pathways can be very different. If the fluid flow is fast, for example in the manuscript the spontaneous imbibition situation ($t_{film} > t_{adv}$), then the displacement pathway is mainly affected by the geometry. On the other hand, if the fluid flow is very slow (providing time for thin films to develop and swell), for example in the manuscript the quasi-static imbibition situation ($t_{film} < t_{adv}$), then the displacement pathway and the pore-filling sequence is likely to follow the filling rules proposed by Lenormand *et al.* (1983), based on the Young–Laplace equation.

Downloaded from https://www.cambridge.org/core. Imperial College London Library, on 05 Sep 2017 at 14:28:43, subject to the Cambridge Core terms of use, available at https://www.cambridge.org/core/terms. https://doi.org/10.1017/jfm.2017.363

The advancement of the invading WP fluid in a real porous medium, under strong wetting conditions, involves two distinct macroscopic fronts (Constantinides & Payatakes 2000; Bico & Quéré 2003). The primary displacement front, which saturates the medium, is due to the piston-type motion of menisci in the main pores. The secondary front is due to the precursor WP films, which propagate ahead of the primary front using the fine structures of the porous material. The distance between the two fronts depends on the capillary number *Ca* and the viscosity ratio and may be many times larger than the mean pore length (Constantinides & Payatakes 2000). Under certain conditions the WP films can swell and cause disconnection and entrapment of the NWP. In these situations the displacement pathways can be significantly different from situations with no WP films. The impact of this phenomenon can be significant. For example Constantinides & Payatakes (2000) report that these WP films cause a substantial increase of the residual NWP saturation. Rücker *et al.* (2015) report on regimes of corner flow and film swelling in real porous media, decreasing the connectivity of the NWP. Micro-fluidic devices and simulations can be used to investigate the dynamics and mechanisms involved in two phase flow at the pore scale and elucidate the role of wettability, viscosity ratio, *Ca* or even roughness using patterned micro-fluidic devices on the advancement of the displacement fronts.

Acknowledgements

This work was conducted as part of the Qatar Carbonates and Carbon Storage Research Centre (QCCSRC), jointly funded by Qatar Petroleum, Shell and the Qatar Science and Technology Park. E.M.C. would also like to acknowledge the Engineering and Physical Sciences Research Council (EPSRC) for their funding.

REFERENCES

ANDERSON, D. M., MCFADDEN, G. B. & WHEELER, A. A. 1998 Diffuse-interface methods in fluid mechanics. *Annu. Rev. Fluid Mech.* **30** (1), 139–165.

BICO, J. & QUÉRÉ, D. 2003 Precursors of impregnation. *Europhys. Lett.* **61** (3), 348–353.

BLUNT, M. J., BIJELJIC, B., DONG, H., GHARBI, O., IGLAUER, S., MOSTAGHIMI, P., PALUSZNY, A. & PENTLAND, C. 2013 Pore-scale imaging and modelling. *Adv. Water Resour.* **51**, 197–216; 35th Year Anniversary Issue.

BLUNT, M. J., JACKSON, M. D., PIRI, M. & VALVATNE, P. H. 2002 Detailed physics, predictive capabilities and macroscopic consequences for pore-network models of multiphase flow. *Adv. Water Resour.* **25** (812), 1069–1089.

BLUNT, M. J. & SCHER, H. 1995 Pore-level modeling of wetting. *Phys. Rev.* E **52** (6), 6387.

BRIANT, A. J. & YEOMANS, J. M. 2004 Lattice Boltzmann simulations of contact line motion. II. Binary fluids. *Phys. Rev.* E **69** (3), 031603.

BRODY, J. P., YAGER, P., GOLDSTEIN, R. E. & AUSTIN, R. H. 1996 Biotechnology at low Reynolds numbers. *Biophys. J.* **71** (6), 3430–3441.

CAHN, J. 1977 Critical-point wetting. *J. Chem. Phys.* **66**, 3367.

CHALBAUD, C., ROBIN, M., LOMBARD, J.-M., MARTIN, F., EGERMANN, P. & BERTIN, H. 2009 Interfacial tension measurements and wettability evaluation for geological CO_2 storage. *Adv. Water Resour.* **32** (1), 98–109.

CHALBAUD, C. A., LOMBARD, J.-M. N., MARTIN, F., ROBIN, M., BERTIN, H. J. & EGERMANN, P. 2007 Two phase flow properties of Brine-CO_2 systems in a carbonate core: influence of wettability on Pc and kr. In *SPE/EAGE Reservoir Characterization and Simulation Conference*. Society of Petroleum Engineers.

Downloaded from https://www.cambridge.org/core. Imperial College London Library, on 05 Sep 2017 at 14:28:43, subject to the Cambridge Core terms of use, available at https://www.cambridge.org/core/terms. https://doi.org/10.1017/jfm.2017.363

CHANG, L.-C., TSAI, J.-P., SHAN, H.-Y. & CHEN, H.-H. 2009 Experimental study on imbibition displacement mechanisms of two-phase fluid using micro model. *Environ. Earth Sci.* **59** (4), 901–911.

CHATENEVER, A. & CALHOUN, J. C. JR. 1952 Visual examinations of fluid behavior in porous media-part I. *J. Petrol. Tech.* **4** (06), 149–156.

CHIQUET, P., BROSETA, D. & THIBEAU, S. 2007 Wettability alteration of caprock minerals by carbon dioxide. *Geofluids* **7** (2), 112–122.

CONSTANTINIDES, G. N. & PAYATAKES, A. C. 2000 Effects of precursor wetting films in immiscible displacement through porous media. *Trans. Porous Med.* **38** (3), 291–317.

COX, R. G. 1986 The dynamics of the spreading of liquids on a solid surface. Part 1. Viscous flow. *J. Fluid Mech.* **168**, 169–194.

D'HUMIÈRES, D., GINZBURG, I., KRAFCZYK, M., LALLEMAND, P. & LUO, L.-S. 2002 Multiple-relaxation-time lattice Boltzmann models in three dimensions. *Phil. Trans. R. Soc. Lond.* A **360**, 437.

DIMITROV, D. I., MILCHEV, A. & BINDER, K. 2007 Capillary rise in nanopores: molecular dynamics evidence for the Lucas–Washburn equation. *Phys. Rev. Lett.* **99**, 054501.

DIOTALLEVI, F., BIFERALE, L., CHIBBARO, S., PONTRELLI, G., TOSCHI, F. & SUCCI, S. 2009 Lattice boltzmann simulations of capillary filling: finite vapour density effects. *Eur. Phys. J. Special Topics* **171** (1), 237–243.

DOUGHTY, C., FREIFELD, B. M. & TRAUTZ, R. C. 2008 Site characterization for CO_2 geologic storage and vice versa: the Frio brine pilot, Texas, USA as a case study. *Environ. Geol.* **54** (8), 1635–1656.

DREYER, M., DELGADO, A. & PATH, H.-J. 1994 Capillary rise of liquid between parallel plates under microgravity. *J. Colloid Interface Sci.* **163** (1), 158–168.

DYMOND, J. H. & ØYE, H. A. 1994 Viscosity of selected liquid *n*-alkanes. *J. Phys. Chem. Ref. Data* **23**, 41–53.

FERRARI, A. & LUNATI, I. 2013 Direct numerical simulations of interface dynamics to link capillary pressure and total surface energy. *Adv. Water Resour.* **57**, 19–31.

GIORDANO, N. & CHENG, J. T. 2001 Microfluid mechanics: progress and opportunities. *J. Phys.: Condens. Matter* **13** (15), R271.

GRAY, F., CEN, J. & BOEK, E. S. 2016 Simulation of dissolution in porous media in three dimensions with lattice Boltzmann, finite-volume, and surface-rescaling methods. *Phys. Rev.* E **94**, 043320.

HECHT, M. & HARTING, J. 2010 Implementation of on-site velocity boundary conditions for D3Q19 lattice Boltzmann simulations. *J. Stat. Mech.* **2010** (01), P01018.

HESSE, M. A., ORR, F. M. & TCHELEPI, H. A. 2008 Gravity currents with residual trapping. *J. Fluid Mech.* **611**, 35–60.

HORNBROOK, J. W., CASTANIER, L. M. & PETTIT, P. A. 1991 Observation of foam/oil interactions in a new high-resolution micromodel. In *SPE Annual Technical Conference and Exhibition*. Society of Petroleum Engineers.

ICHIKAWA, N., HOSOKAWA, K. & MAEDA, R. 2004 Interface motion of capillary-driven flow in rectangular microchannel. *J. Colloid Interface Sci.* **280** (1), 155–164.

ICHIKAWA, N. & SATODA, Y. 1994 Interface dynamics of capillary flow in a tube under negligible gravity condition. *J. Colloid Interface Sci.* **162** (2), 350–355.

KARADIMITRIOU, N. K. & HASSANIZADEH, S. M. 2012 A review of micromodels and their use in two-phase flow studies. *Vadose Zone Journal* **11** (3).

KAVEHPOUR, H. P., OVRYN, B. & MCKINLEY, G. H. 2003 Microscopic and macroscopic structure of the precursor layer in spreading viscous drops. *Phys. Rev. Lett.* **91** (19), 196104.

KENDON, V. M., CATES, M. E., PAGONABARRAGA, I., DESPLAT, J.-C. & BLADON, P. 2001 Inertial effects in three-dimensional spinodal decomposition of a symmetric binary fluid mixture: a lattice boltzmann study. *J. Fluid Mech.* **440**, 147–203.

KUHN, H., FÖRSTERLING, H.-D. & WALDECK, D. H. 2009 *Principles of Physical Chemistry*. Wiley.

KUMAR GUNDA, N. S., BERA, B., KARADIMITRIOU, N. K., MITRA, S. K. & HASSANIZADEH, S. M. 2011 Reservoir-on-a-chip (roc): a new paradigm in reservoir engineering. *Lab on a Chip* **11** (22), 3785–3792.

Downloaded from https://www.cambridge.org/core. Imperial College London Library, on 05 Sep 2017 at 14:28:43, subject to the Cambridge Core terms of use, available at https://www.cambridge.org/core/terms. https://doi.org/10.1017/jfm.2017.363

KUSUMAATMAJA, H., POOLEY, C. M., GIRARDO, S., PISIGNANO, D. & YEOMANS, J. M. 2008 Capillary filling in patterned channels. *Phys. Rev.* E **77**, 067301.

LALLEMAND, P. & LUO, L.-S. 2000 Theory of the lattice Boltzmann method: dispersion, dissipation, isotropy, Galilean invariance, and stability. *Phys. Rev.* E **61**, 6546–6562.

LENORMAND, R. 1990 Liquids in porous media. *J. Phys.: Condens. Matter* **2** (S), SA79.

LENORMAND, R., ZARCONE, C. & SARR, A. 1983 Mechanisms of the displacement of one fluid by another in a network of capillary ducts. *J. Fluid Mech.* **135**, 337–353.

LEVINE, S., LOWNDES, J., WATSON, E. J. & NEALE, G. 1980 A theory of capillary rise of a liquid in a vertical cylindrical tube and in a parallel-plate channel: Washburn equation modified to account for the meniscus with slippage at the contact line. *J. Colloid Interface Sci.* **73** (1), 136–151.

LUCAS, R. 1918 Rate of capillary ascension of liquids. *Kolloidn.* Z **23** (15), 15–22.

LYONS, W. 2009 *Working Guide to Reservoir Engineering*. Gulf Professional Publishing.

MOGNETTI, B. M. & YEOMANS, J. M. 2009 Capillary filling in microchannels patterned by posts. *Phys. Rev.* E **80**, 056309.

MORROW, N. R. & MASON, G. 2001 Recovery of oil by spontaneous imbibition. *Curr. Opin. Colloid Interface Sci.* **6** (4), 321–337.

ØREN, P.-E. & BAKKE, S. 2003 Reconstruction of berea sandstone and pore-scale modelling of wettability effects. *J. Petrol. Science Engineering* **39** (3), 177–199.

ØREN, P.-E., BAKKE, S. & ARNTZEN, O. J. 1998 Extending predictive capabilities to network models. *SPE J. RICHARDSON* **3**, 324–336.

PETRASH, D. A., NELSON, T. M. & OTTO, E. W. 1963 *Effect of Surface Energy on the Liquid–Vapor Interface Configuration During Weightlessness*. National Aeronautics and Space Administration.

POOLEY, C. M., KUSUMAATMAJA, H. & YEOMANS, J. M. 2008 Contact line dynamics in binary lattice Boltzmann simulations. *Phys. Rev.* E **78**, 056709.

POOLEY, C. M., KUSUMAATMAJA, H. & YEOMANS, J. M. 2009 Modelling capillary filling dynamics using lattice Boltzmann simulations. *Eur. Phys. J. Special Topics* **171** (1), 63–71.

QUÉRÉ, D. 1997 Inertial capillarity. *Europhys. Lett.* **39** (5), 533.

RAISKINMÄKI, P., SHAKIB-MANESH, A., JÄSBERG, A., KOPONEN, A., MERIKOSKI, J. & TIMONEN, J. 2002 Lattice-Boltzmann simulation of capillary rise dynamics. *J. Stat. Phys.* **107** (1–2), 143–158.

RANGEL-GERMAN, E. R. & KOVSCEK, A. R. 2006 A micromodel investigation of two-phase matrix-fracture transfer mechanisms. *Water Resour. Res.* **42**, W03401.

ROWLINSON, J. S. & WIDOM, B. 1982 *Molecular Theory of Capillarity*. Clarendon.

RÜCKER, M., BERG, S., ARMSTRONG, R. T., GEORGIADIS, A., OTT, H., SCHWING, A., NEITELER, R., BRUSSEE, N., MAKURAT, A., LEU, L. *et al.* 2015 From connected pathway flow to ganglion dynamics. *Geophys. Res. Lett.* **42** (10), 3888–3894.

SAADATPOOR, E., BRYANT, S. L. & SEPEHRNOORI, K. 2011 Effect of upscaling heterogeneous domain on CO_2 trapping mechanisms. *Energy Procedia* **4** (0), 5066–5073; 10th International Conference on Greenhouse Gas Control Technologies.

SEMPREBON, C., KRÜGER, T. & KUSUMAATMAJA, H. 2016 Ternary free-energy lattice Boltzmann model with tunable surface tensions and contact angles. *Phys. Rev.* E **93**, 033305.

SHENG, P. & ZHOU, M. 1992 Immiscible-fluid displacement: contact-line dynamics and the velocity-dependent capillary pressure. *Phys. Rev.* A **45** (8), 5694.

SIEGEL, R. 1961 Transient capillary rise in reduced and zero-gravity fields. *Trans. ASME J. Appl. Mech.* **28** (2), 165–170.

SORBIE, K. S. & SKAUGE, A. 2012 Can network modeling predict two-phase flow functions. *Petrophysics* **53** (06), 401–409.

STANGE, M., DREYER, M. E. & RATH, H. J. 2003 Capillary driven flow in circular cylindrical tubes. *Phys. Fluids* **15** (9), 2587–2601.

STUKAN, M. R., LIGNEUL, P., CRAWSHAW, J. P. & BOEK, E. S. 2010 Spontaneous imbibition in nanopores of different roughness and wettability. *Langmuir* **26** (16), 13342–13352.

TAKU, I. S., JESSEN, K. & ORR, F. M. JR. 2007 Storage of CO_2 in saline aquifers: effects of gravity, viscous, and capillary forces on amount and timing of trapping. *Intl J. Greenh. Gas Control* **1** (4), 481–491.

Downloaded from https://www.cambridge.org/core. Imperial College London Library, on 05 Sep 2017 at 14:28:43, subject to the Cambridge Core terms of use, available at https://www.cambridge.org/core/terms. https://doi.org/10.1017/jfm.2017.363

TOKUNAGA, T. K., WAN, J., JUNG, J.-W., KIM, T. W., KIM, Y. & DONG, W. 2013 Capillary pressure and saturation relations for supercritical CO_2 and brine in sand: high-pressure Pc(Sw) controller/meter measurements and capillary scaling predictions. *Water Resour. Res.* **49** (8), 4566–4579.

VALVATNE, P. H. & BLUNT, M. J. 2003 Predictive pore-scale network modeling. In *SPE Annual Technical Conference and Exhibition*. Society of Petroleum Engineers.

VALVATNE, P. H. & BLUNT, M. J. 2004 Predictive pore-scale modeling of two-phase flow in mixed wet media. *Water Resour. Res.* **40** (7), w07406.

VIZIKA, O., AVRAAM, D. G. & PAYATAKES, A. C. 1994 On the role of the viscosity ratio during low-Capillary-number forced imbibition in porous media. *J. Colloid Interface Sci.* **165** (2), 386–401.

WASHBURN, E. W. 1921 The dynamics of capillary flow. *Phys. Rev.* **17** (3), 273.

YEOMANS, J. M. 2006 Mesoscale simulations: lattice Boltzmann and particle algorithms. *Physica* A **369** (1), 159–184.

YU, L. & WARDLAW, N. C. 1986 Mechanisms of nonwetting phase trapping during imbibition at slow rates. *J. Colloid Interface Sci.* **109** (2), 473–486.

ZACHAROUDIOU, I. & BOEK, E. S. 2016 Capillary filling and Haines jump dynamics using free energy Lattice Boltzmann simulations. *Adv. Water Resour.* **92**, 43–56.

ZHMUD, B. V., TIBERG, F. & HALLSTENSSON, K. 2000 Dynamics of capillary rise. *J. Colloid Interface Sci.* **228** (2), 263–269.

Downloaded from https://www.cambridge.org/core. Imperial College London Library, on 05 Sep 2017 at 14:28:43, subject to the Cambridge Core terms of use, available at https://www.cambridge.org/core/terms. https://doi.org/10.1017/jfm.2017.363